submitted to *Geophys. J. Int.*

# Supplementary material for "Constraints on the resistivity of the oceanic lithosphere and asthenosphere from seafloor ocean tidal electromagnetic measurements"

H. Zhang[1,2], G. D. Egbert[2], A. D. Chave[3], Q. Huang[1⋆] and A. Kelbert[4] and S. Y. Erofeeva[2]

[1] *School of Earth and Space Sciences, Peking University, Beijing, China.*

[2] *College of Earth, Ocean, and Atmospheric Sciences, Oregon State University, OR, USA.*

[3] *Department of Applied Ocean Physics and Engineering, Woods Hole Oceanographic Institution, MA, USA.*

[4] *USGS Geomagnetism Program, Golden, CO, USA.*

27 June 2019

**Estimate the OTEM signal**

The inner loop described in Section 6 addresses the over parameterized problem:

$$\mathbf{y} = \mathbf{X} \cdot \beta + \epsilon \tag{S1}$$

where $\mathbf{y}$ is a response N-vector of hourly means of a single component of data, $\mathbf{X}$ is given by Eq.S2, $\beta$ is a $2p+1$ vector of parameters and $\epsilon$ is an N-vector of random errors. The transpose of the $N \times (2p+1)$ predictor matrix $\mathbf{X}^T$ is given by

$$\mathbf{X}^T = \begin{bmatrix} f_1(t_0)cos(\omega_1 t_0 + \phi_1 + u_1(t_0)) & \cdots & f_1(t_{N-1})cos(\omega_1 t_{N-1} + \phi_1 + u_1(t_{N-1})) \\ \vdots & \vdots & \vdots \\ f_p(t_0)cos(\omega_p t_0 + \phi_p + u_p(t_0)) & \cdots & f_p(t_{N-1})cos(\omega_p t_{N-1} + \phi_p + u_p(t_{N-1})) \\ f_1(t_0)sin(\omega_1 t_0 + \phi_1 + u_1(t_0)) & \cdots & f_1(t_{N-1})sin(\omega_1 t_{N-1} + \phi_1 + u_1(t_{N-1})) \\ \vdots & \vdots & \vdots \\ f_p(t_0)sin(\omega_p t_0 + \phi_p + u_p(t_0)) & \cdots & f_p(t_{N-1})sin(\omega_p t_{N-1} + \phi_p + u_p(t_{N-1})) \\ 1 & \cdots & 1 \end{bmatrix} \tag{S2}$$

where $f_i(t_j)$ and $u_i(t_j)$ are the nodal modulation amplitude and phase for the i-th tidal species at the j-th time point expressed as modified Julian day. If nodal modulations are not available, $f_i$ and $u_i$ are set to 1 and 0, respectively. The variables $\phi$ are the phase shifts relative to 1 Jan 1992 at 0000 UT.

Once the solution of Eq.S1 has been obtained, we compute the multi-taper power spectrum of the residuals resulting from removal of all of the lines in $\mathbf{y}$. The residual power spectrum at the period of each line is used to compute the corresponding residual variance $\hat{\sigma}_i^2$. Each line is then assessed using the hypothesis test H0: $\hat{\mu}_i = 0$ vs H1: $\hat{\mu}_i > 0$. At each outer iteration, the set of line periods is culled of those values corresponding to p-values greater than 0.05 and the entire procedure is repeated. The procedure terminates when all of the p-values are below 0.05, which typically takes 2-4 iterations. When the iterative procedure described above is finished, confidence intervals are placed on the amplitudes and phases using a percentile bootstrap approach. A set of

980 bootstrap replicates of the final predictor matrix and robust weights, along with the data, are obtained by random sampling with replacement. The weighted least squares solution is obtained for each line, and the total tail probability is 0.05, since it is apportioned equally between the amplitude and phase.

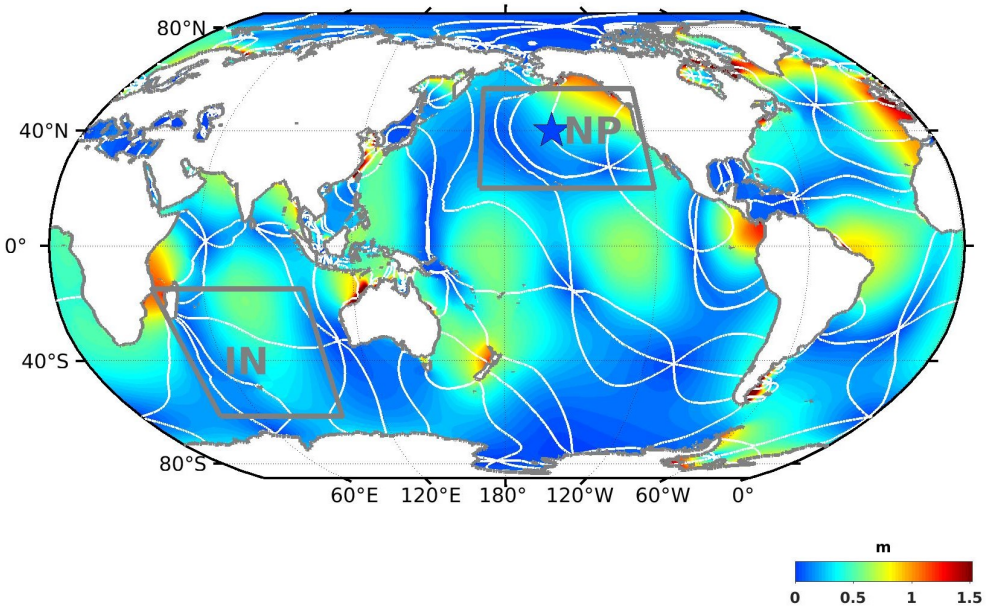


**Figure S1.** The sea surface height variation and phase of M2 tidal constituent predicted by TPXO8 (Egbert & Erofeeva 2002). The cotidal lines (white lines) are spaced at phase interval of 60°.

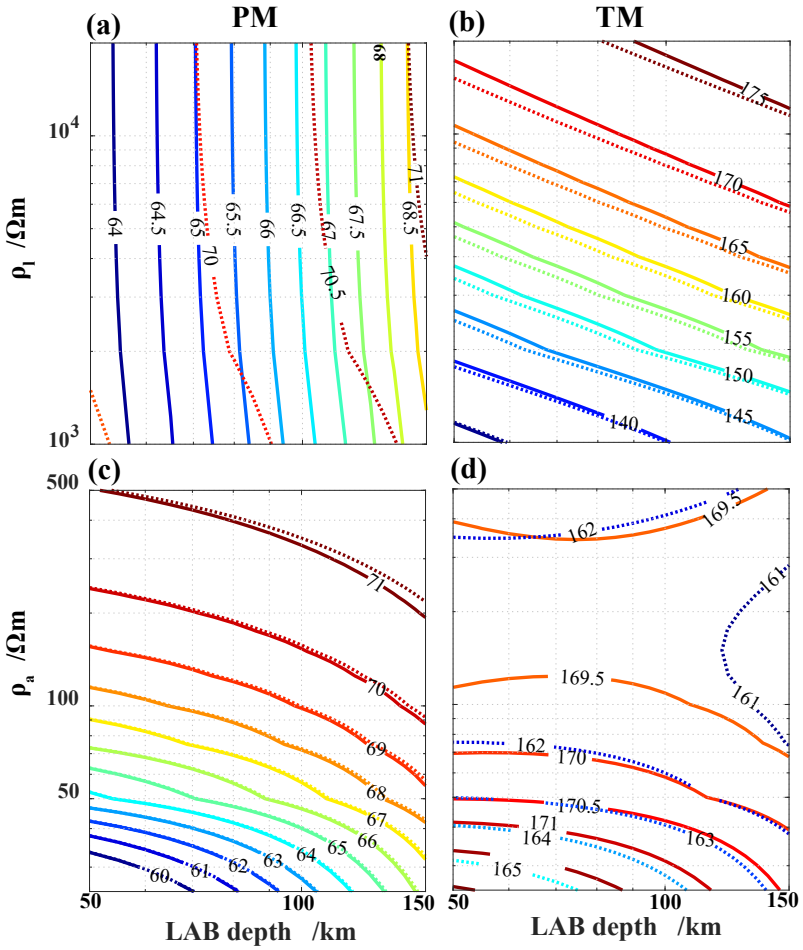


**Figure S2.** Contour plot of phase of PM (left column) and TM (right column) response function varying with (a)-(b) lithospheric resistivity $\rho_l$ and the LAB depth. The solid and dotted contours are for models in which $\rho_a$ is 50 and 200 $\Omega m$, respectively. The black dashed line in b denotes the line $\rho_l H_l = const.$ (c)-(d) asthenospheric resistivity $\rho_a$ and the LAB depth with fixed lithospheric resistance $\rho_l H_l$. The solid and dotted contours are for models in which the resistance is $8 \times 10^8 \Omega m^2$ and $4 \times 10^8 \Omega m^2$, respectively.

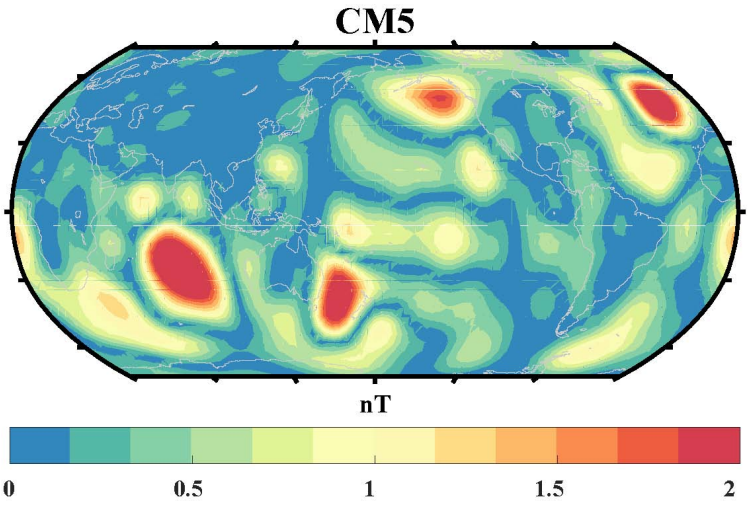


**Figure S3.** The amplitude of satellite $B_z$ component in geomagnetic model CM5 (Sabaka et al., 2015).

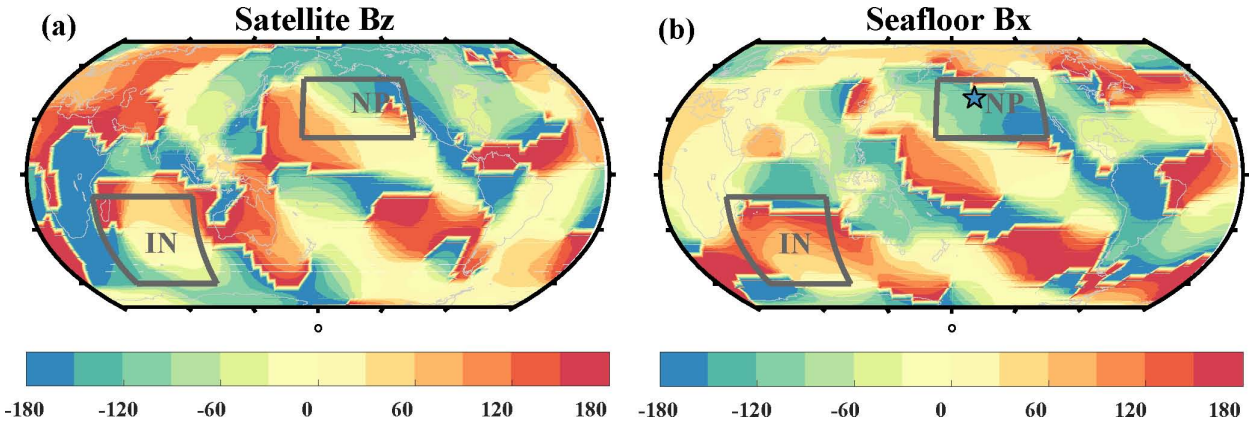


**Figure S4.** The phase of the M2 OTEM field. (a) The vertical magnetic component $B_z$ at satellite altitude (430 km) (b) The north magnetic component $B_x$ on the seafloor.

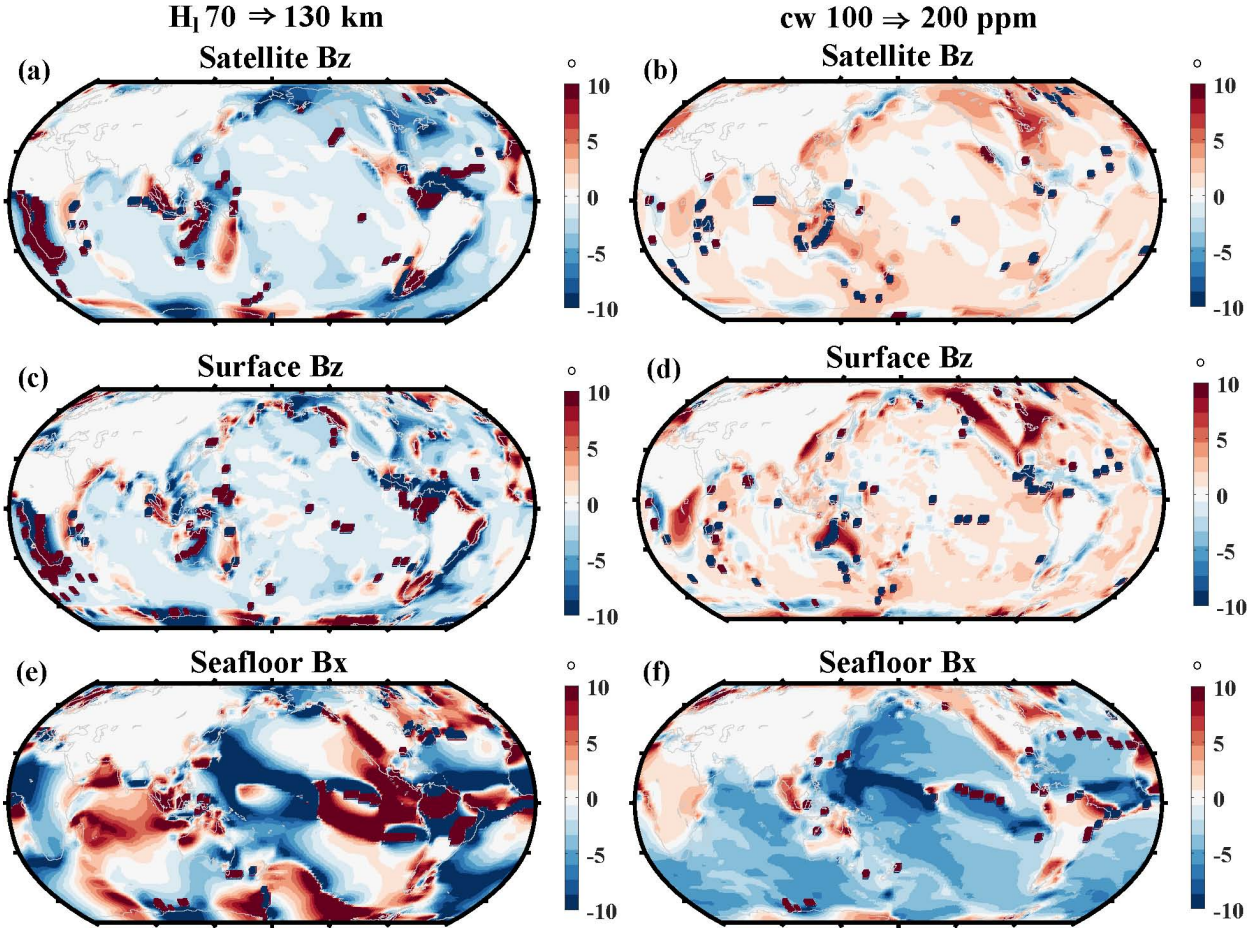


**Figure S5.** Changes in the phase of magnetic signal when the LAB depth increases from 70 to 130 km (the left column), and the mantle water content increases from 100 to 200 ppm (the right column). (a)-(b) The vertical magnetic signal $B_z$ at satellite altitude. (c)-(d) The vertical magnetic signal $B_z$ on the Earth's surface. (e)-(f) The north component $B_x$ on the seafloor. Note that the scattered outliers are located in regions where the amplitude and phase are small, so a fluctuation in the real or imaginary part of magnetic field can result in large phase shift, but the modeling results are still reliable.

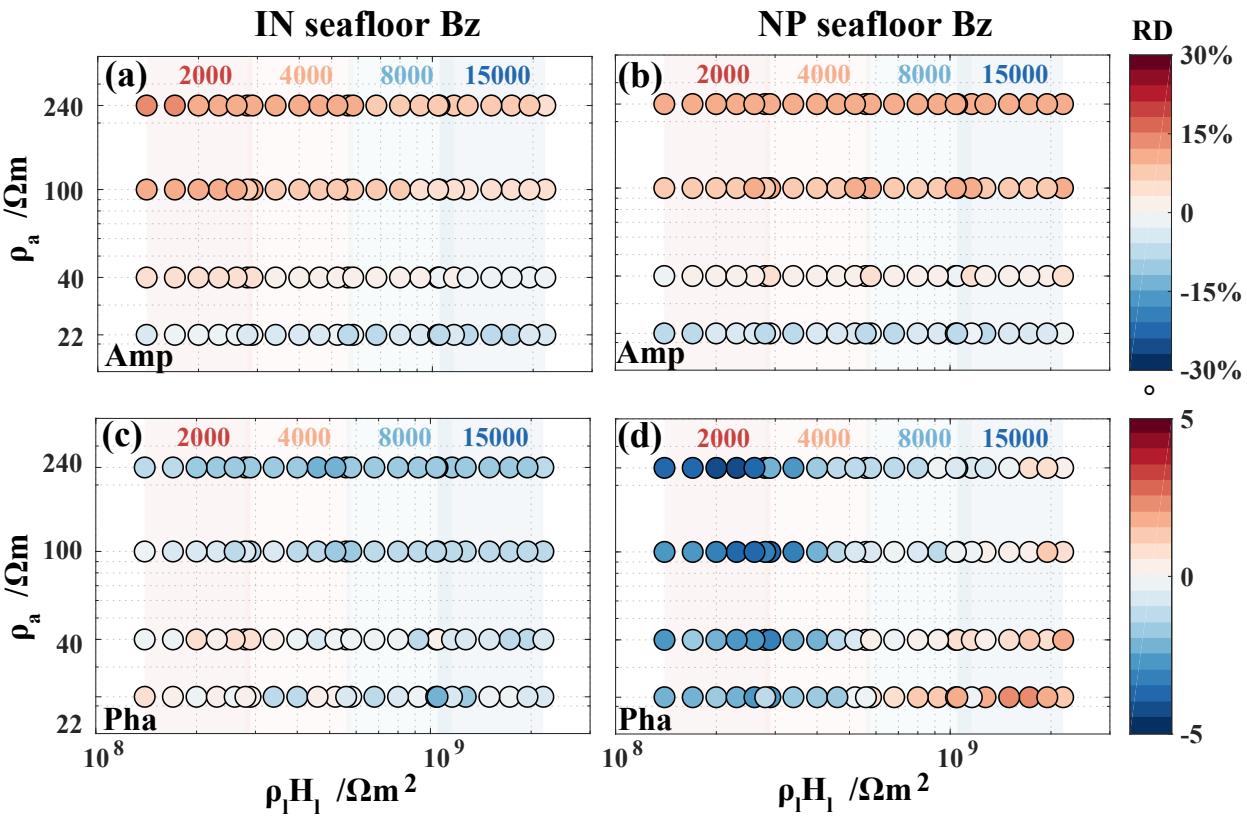


**Figure S6.** The pseudocolor plot of seafloor $B_z$ component in the Indian Ocean (left column) and northeastern Pacific (right column) as a function of $\rho_a$ and $\rho_l H_l$. (a)-(b) The relative difference in amplitude. (c)-(d) The absolute differences in phase. Other symbols are similar to Fig. 9 in the main text.

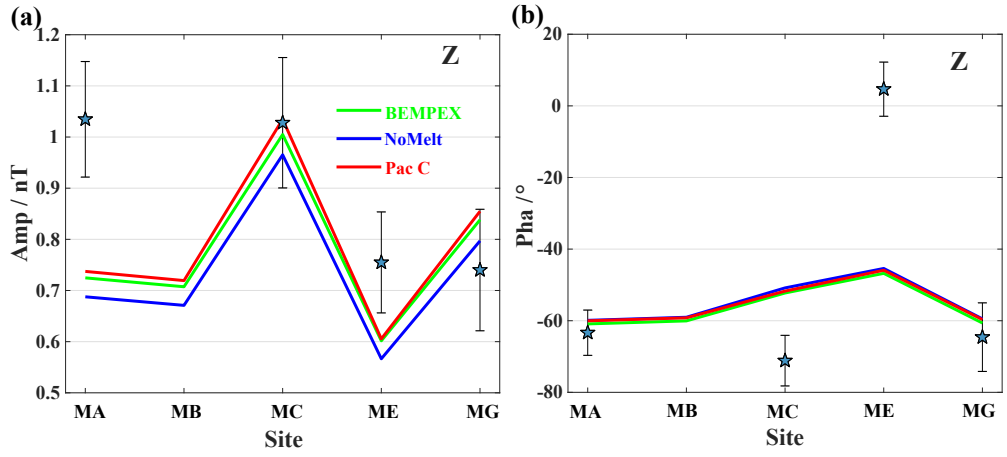


**Figure S7.** The observed versus predicted magnetic signal at BEMPEX seafloor stations. (a) The amplitude of $Z$. (b) The phase of $Z$. Symbols are same with Fig. 13.

## REFERENCES

Egbert, G. D. & Erofeeva, S. Y.(2002). Efficient inverse modeling of barotropic ocean tides. Journal of Atmospheric and Oceanic Technology, 19(2), 183–204.

Sabaka, T. J., Olsen, N., Tyler, R. H., & Kuvshinov, A.(2015). CM5, a pre-Swarm comprehensive geomagnetic field model derived from over 12 yr of CHAMP, Ørsted, SAC-C and observatory data. Geophysical Journal International, 200(3), 1596-1626.